

Thermal FEM Analysis of Surge Arresters during HVDC Current Interruption Validated by Experiments

Liu, S.; Popov, M.; Belda, Nadew; Smeets, Rene; Liu, Zhiyuan

DOI

[10.1109/TPWRD.2021.3086673](https://doi.org/10.1109/TPWRD.2021.3086673)

Publication date

2022

Document Version

Final published version

Published in

IEEE Transactions on Power Delivery

Citation (APA)

Liu, S., Popov, M., Belda, N., Smeets, R., & Liu, Z. (2022). Thermal FEM Analysis of Surge Arresters during HVDC Current Interruption Validated by Experiments. *IEEE Transactions on Power Delivery*, 37(3), 1412-1422. Article TPWRD-00966-2020. <https://doi.org/10.1109/TPWRD.2021.3086673>

Important note

To cite this publication, please use the final published version (if applicable). Please check the document version above.

Copyright

Other than for strictly personal use, it is not permitted to download, forward or distribute the text or part of it, without the consent of the author(s) and/or copyright holder(s), unless the work is under an open content license such as Creative Commons.

Takedown policy

Please contact us and provide details if you believe this document breaches copyrights. We will remove access to the work immediately and investigate your claim.






Green Open Access added to TU Delft Institutional Repository

'You share, we take care!' - Taverne project

<https://www.openaccess.nl/en/you-share-we-take-care>

Otherwise as indicated in the copyright section: the publisher is the copyright holder of this work and the author uses the Dutch legislation to make this work public.

Thermal FEM Analysis of Surge Arresters During HVdc Current Interruption Validated by Experiments

Siyuan Liu , *Member, IEEE*, Marjan Popov , *Senior Member, IEEE*, Nadew Adisu Belda , *Member, IEEE*, René Peter Paul Smeets , *Fellow, IEEE*, and Zhiyuan Liu , *Senior Member, IEEE*

Abstract—This paper deals with the development of an accurate finite-element model of an arrester to investigate the electrothermal and mechanical stress during dc current interruption. The comprehensive analysis performed on a ZnO surge arrester is supported by experiments during high-voltage dc circuit breaker current interruption. The performed experimental analysis comprises three sequential 26 kV/10 kA direct current interruption tests carried out within a period of one hour. The dynamic temperature and current distribution of the surge arrester columns during current interruption are measured. The finite-element simulation results are in good agreement with the test results. The influence of the surge arrester temperature on the current distribution among the surge arrester columns is analyzed. The impact of the surge arrester temperature on ZnO electrical characteristics and mechanical stress inside the surge arrester are also investigated. The surge arrester finite-element model can be used with full success for parameter optimization of the surge arresters to prevent possible failures when dc circuit breakers performed multiple interruptions in short period of time.

Index Terms—Metal-oxide surge arresters, dc circuit breaker, thermodynamics finite-element simulation, temperature measurement.

I. INTRODUCTION

THE prompt development of voltage source converters paves the way towards building multi-terminal dc grids, which will be used for the connection of offshore wind power

Manuscript received June 27, 2020; revised February 2, 2021 and April 1, 2021; accepted June 2, 2021. Date of publication June 4, 2021; date of current version May 24, 2022. This work was supported by European Commission under Grant 691714 “Progress on Meshed HVdc Offshore Transmission Networks” through Horizon 2020 programme and by the China National Postdoctoral Program for Innovative Talents under Grant BX20200263. Paper no. TPWRD-00966-2020. (*Corresponding author: Marjan Popov.*)

Siyuan Liu is with the Department of Electrical Engineering, State Key Laboratory of Electrical Insulation and Power Equipment, Xi’an Jiaotong University, Xi’an 710049, China, and also with the Faculty of EEMCS, Delft University of Technology, Mekelweg, 2628CD Delft, The Netherlands (e-mail: siyuanliu@xjtu.edu.cn).

Marjan Popov is with the Faculty of EEMCS, Delft University of Technology, Mekelweg, 2628CD Delft, The Netherlands (e-mail: m.popov@tudelft.nl).

Nadew Adisu Belda and René Peter Paul Smeets are with Kema Labs, Klingelbeekseweg, 6812DE Arnhem, The Netherlands (e-mail: nadew.belda@kema.com; rene.smeets@kema.com).

Zhiyuan Liu is with the Department of Electrical Engineering, State Key Laboratory of Electrical Insulation and Power Equipment, Xi’an Jiaotong University, Xi’an 710049, China (e-mail: liuzy@mail.xjtu.edu.cn).

Color versions of one or more figures in this article are available at <https://doi.org/10.1109/TPWRD.2021.3086673>.

Digital Object Identifier 10.1109/TPWRD.2021.3086673

plants [1]–[3]. One of the main bottlenecks for developing multi-terminal dc grids is the lack of fast, economical and reliable high-voltage dc (HVdc) circuit breakers (CBs) [4]. The dc CBs are required to isolate the faulted segments of the multi-terminal dc grid in several milliseconds in order to keep the healthy segments operating continuously [5]. So far, several dc CB concepts have been developed and reported as suitable solutions for (HVdc) current interruption [6]–[13].

Current interruption in multi-terminal dc grids is far more complicated than the current interruption in well-known ac CBs because of not having current zero in a dc system [11]. All HVdc CB technologies operate on the principle of creating a counter voltage known as transient interruption voltage. To achieve this dc CBs employ several current branches with different components serving different purposes as illustrated in Fig. 1 [14]. Firstly, the current is interrupted locally in the main current branch leading to the current commutation into the parallel current commutation branch. This TIV is produced in the commutation branch and is limited by the energy absorption branch in the third parallel branch. All the dc CBs have a metal oxide surge arrester (MOSA), which is used to limit the transient interruption voltage and absorb the energy stored in the system.

Therefore, the MOSA is a very crucial component of the dc CBs as it deals with the absorption of large amount of energy resulting from the fault current interruption [15]. In dc CBs, the MOSAs are part of the dc CBs themselves, and their task is to absorb the energy stored in the lines or cables and converters during the current is interruption process. The amount of energy (which may be in a range of several megajoules) and the very short period of time in which this energy should be removed (5–10 milliseconds), makes the temperature rise faster and much higher. As a result, the evaluation of the thermal stress during and after the dc interruption is very important for the MOSAs in dc CBs. Particularly for the future overhead multi-terminal dc grid, reclosing operation is essential for the protection strategy, which leads to multiple dc interruptions and hence multiple energy absorptions in a short duration [16].

So far, there has been no testing platform that could provide test environment for the open-close-open current interruption while applying full energy in a short period of time in the order of 300 ms. As a result, an accurate finite-element (FE) model is a suitable method to investigate electrothermal-mechanical behavior of a MOSA during multiple dc interruptions. The validated model can be used to simulate different scenarios of DC current interruption such as reclosing operation

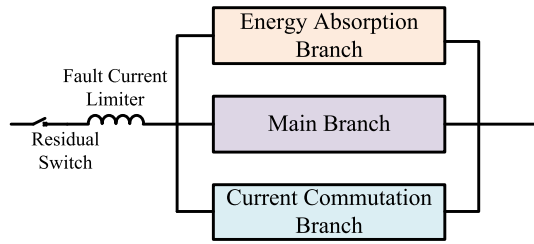


Fig. 1. Generic model of HVdc circuit breakers.

(open-close-open) and other multiple current interruptions in multi-terminal dc grids. Extensive research has been conducted on the thermal and mechanical stability of MOSAs [17]–[22]. So far, vast majority of studies have been focused on failure analysis of single MOSA column or zinc oxide (ZnO) varistor blocks. Besides, experimental research on the MOSAs during successive dc interruptions and associated temperature impact on the current distribution and mechanical stress among parallel columns comprising the full MOSA of the dc CB has been rarely reported.

The failure modes of the MOSAs can be divided as a thermal runaway, a puncture, and cracking, and are discussed in [22], [23]. The thermal runaway strongly depends on current and voltage instability, which usually occurs in the MOSAs applied in ac over-voltage protection. It occurs when the heating generated by the leakage current exceeds the heat dissipation and MOSA temperature exceeds the thermal stability point [23]. Puncture is caused by localized current flow in the microstructure of the ZnO disks [17]. Meanwhile, in the breakdown regime, the current density in a ZnO varistor is inhomogeneous [24]. The current in this operating region forms channels and paths through the ceramics and does not flow homogeneously [25]. Besides, inhomogeneous current leads to uneven heat generation, resulting in inhomogeneous thermal expansion in the MOSAs, which is the main reason for cracking failure [26]. During the conducting period of the ZnO varistor, energy is injected accordingly, which can be seen as an adiabatic process due to a temperature rise, which results in thermal stresses inside the ZnO varistor. If the thermal stresses exceed the critical value, cracking of varistor disks takes place.

In practice, MOSA consists of large number of parallel columns to deal with large amount of energy absorption. During the current suppression period (lasting 5–10 ms) of the interruption process, the temperature of the MOSA rises to high value and thereafter begins to cool down. The thermal diffusion of the MOSA columns depends on the MOSA's thermal conductivity, the ambient temperature, and the convection losses. The temperature of the MOSA columns decays slowly after the dc interruption. Due to physical arrangement of the MOSA columns, the columns near the outer edges cool faster than the columns located in the inner side of the MOSA bank. The unequal temperature distribution may lead to the unequal current distribution among these columns. The hotter columns in the middle have higher conductivity because of the negative correlation between the conductivity of zinc oxide and its temperature. Therefore, more current will flow through the hotter

TABLE I
SURGE ARRESTER COLUMNS MATCHING RESULTS

/kV	Column1	Column2	Column3	Column4	Column5	Column6
Layer1	7.35	7.36	7.35	7.36	7.35	7.35
Layer 2	7.38	7.38	7.37	7.37	7.36	7.37
Layer 3	7.39	7.39	7.38	7.39	7.38	7.39
Layer 4	7.40	7.40	7.41	7.40	7.41	7.40
Layer 5	7.41	7.41	7.42	7.42	7.43	7.42
Layer 6	7.44	7.43	7.44	7.43	7.44	7.44
Total	44.37	44.37	44.37	44.37	44.37	44.37

columns, which may lead to overheating of the MOSA or even a failure in the dc current interruption. Therefore, the analysis thermal stress on the MOSAs during the dc current interruption is very important for the design of dc CBs. So far, no research has been done on the MOSA thermal stress during dc current interruption.

The remainder of the paper is organized as follows. Section II deals with the physical modelling of MOSAs in a 3D environment with FE. The experimental setup and the detailed measurement are demonstrated in Section III. In Section IV, the MOSA model is validated by experimental measurements and the results are analyzed. The paper ends up with meaningful conclusions based on the obtained results.

II. ELECTROTHERMAL-MECHANICAL MODEL OF MOSA

A. Thermal Model of the MOSA

Thermal analysis of MOSA deal with heat diffusion. Current conduction of MOSA during the current suppression period leads to huge Joule losses, which results in a large amount of heat generation inside the ZnO varistor blocks. The heat generation is a transient process and its propagation in the MOSA during a given time interval can be described in coordinates by the following equations:

Equation (1) represents the transient heat conduction process,

$$\nabla \cdot (k \nabla T) + Q_v = \rho C_p \frac{\partial T}{\partial t} \quad (1)$$

$$Q_v = \begin{cases} E_{SA}/V & \text{(Internal)} \\ E_{SA}/V + Q_r & \text{(Surface)} \end{cases} \quad (2)$$

where k is the heat conductivity, T is the absolute temperature.

Q_v is the heat generated per unit volume. For ZnO varistors inside the SA, the heat source is the Joule heat generated during the energy absorption (E_{SA}), which is calculated by equation (15). Meanwhile, for the ZnO varistors on the surface, the heat source is the Joule heat plus radiation heat. As a result, Q_v can be expressed as (2). C_p and ρ are the heat capacity and mass density, respectively and t is the time; Both k , C_p and ρ are functions of temperature, the functions can be found in Table III.

$$-k \frac{\partial T}{\partial r} \Big|_{\text{Surface}} = h(T_{\text{suf}} - T_{\text{amb}}) \quad (3)$$

Equation (3) is known as heat convection equation, with T_{suf} and T_{amb} being the ZnO varistor surface temperature and ambient temperature. In present work, it is assumed that the

TABLE II
GEOMETRY PARAMETERS OF SURGE ARRESTER

	Diameters(mm)	Height(mm)
Varistors	99	21.4
Spacers	100	5
Top fastener	99	10
Bottom fastener	34	30

TABLE III
CHARACTERISTICS OF MATERIALS

	Mass density ρ (kg/m ³)
ZnO Varistor	$5672-1.4 \times 10^{-3}T-1.5 \times 10^{-4}T^2-7.6 \times 10^{-8}T^3$
Aluminum	$2736.9-2.8 \times 10^{-2}T-1.0 \times 10^{-3}T^2-71.7 \times 10^{-5}T^3$
Brass Type 2600	$8627.3-7.2 \times 10^{-2}T-3.1 \times 10^{-3}T^2-8.4 \times 10^{-6}T^3$
	Heat capacity C_p (J/(kg·K))
ZnO Varistor	$41.6+3T-6.8 \times 10^{-3}T^2+7.3 \times 10^{-6}T^3-3 \times 10^{-9}T^4$
Aluminum	$595.7+1.5T-2.1 \times 10^{-3}T^2+1.3 \times 10^{-6}T^3$
Brass Type 2600	373
	Thermal conductivity k (W/(m·K))
ZnO Varistor	$255.5-1.7T+6.5 \times 10^{-3}T^2-1.4 \times 10^{-5}T^3$
Aluminum	$39.6+1.7T-5.4 \times 10^{-3}T^2+8.4 \times 10^{-6}T^3$
Brass Type 2600	$3.7-0.8T-1.8 \times 10^{-2}T^2+2.3 \times 10^{-6}T^3$

ambient temperature T_{amb} is constant. The heat convection occurs between ZnO varistor surface and the natural air in ambient environment. h is the natural convection coefficient in air and it can be estimated by (4) [27].

$$h = \frac{k}{L} C (Gr \cdot Pr)^n \quad (4)$$

$$Gr = \frac{g\varphi(T_{suf} - T_{amb})L^3}{\nu^2} \quad (5)$$

$$Pr = \frac{\nu}{\zeta} \quad (6)$$

$$\varphi = \frac{1}{T_{suf}} \quad (7)$$

$$\zeta = \frac{k_{air}}{C_{p,air}\rho_{air}} \quad (8)$$

$$Q_r = \varepsilon\sigma A(T_{suf}^4 - T_{amb}^4) \quad (9)$$

The characteristic length L in equation (4) for the cylinder is calculated by $L = \pi R^2 l / 2\pi R l = R/2$, where R and l is the radius and height of the ZnO varistor, respectively. And for the flat plate $L = bl$, where b and l are the broadness and height of the plate. C and n are constants determined by the shape of the varistor surface, respectively. For the vertically positioned cylinders, C is chosen as 0.99 and n is chosen as 0.33. Gr is Grashof number as computed by (5), whilst Prandtl number Pr is determined by (6). Other parameters are: g - gravitational acceleration, $g = 9.8 \text{ m/s}^2$, β - volume expansion coefficient for the surrounding air, φ can be calculated by (7), ν is kinematic viscosity (for air, $\nu = 14.8 \times 10^{-6} \text{ m}^2/\text{s}$), ζ is thermal diffusivity, for air, ζ is determined by (8). Hence, by combining equations (4)-(8), the h is found to be in the range of $5 \sim 6 \text{ W}/(\text{m}^2 \cdot \text{K})$ under the temperature range of $10 \sim 100 \text{ }^\circ\text{C}$.

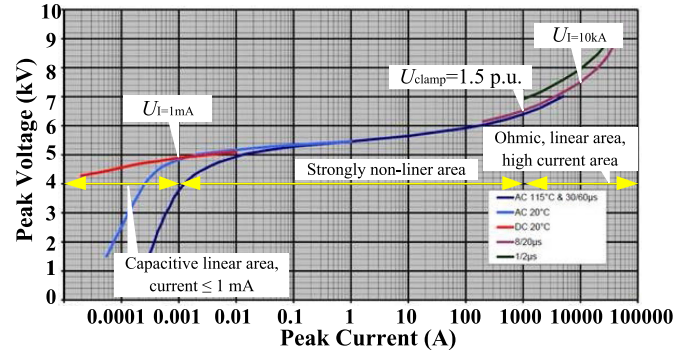


Fig. 2. The V-I characteristic of the ZnO varistor blocks used in the experiment.

Equation (9) determines the process of thermal radiation where Q_r is the radiation heat flux. ε is the emissivity, and the emissivity of ZnO varistor is 0.83. σ is the Stefan-Boltzmann constant, $\sigma = 5.67 \times 10^{-8} \text{ W}/(\text{m}^2 \cdot \text{K}^4)$. A is the radiating surface area.

B. Surge Arrester Thermal Stress

The cracking of ZnO varistors caused by energy absorption is investigated through thermal mechanics. Assuming E_e is amount of energy that is absorbed by a ZnO element, the adiabatic emperature rise can be computed by (10):

$$E_e = \Delta V \cdot \int \rho(T) C_p(T) dT \quad (10)$$

where ΔV denotes the ZnO element volume with a specific mass density ρ at particular temperature T . Furthermore, C_p is the specific thermal capacity of ZnO varistor at temperature T . If the temperatures rise of two close elements are denoted by ΔT_a and ΔT_b respectively, the thermal stress F between the two elements can be computed by (11):

$$F = \frac{Ea(\Delta T_a - \Delta T_b)}{1 - \mu} \quad (11)$$

where E is Young's module of elasticity, and μ is Poisson's ratio; a is the linear expansion coefficient in units of $1/\text{K}$, which is a function of temperature [23] that can be expressed by $a = (-a_1 - a_2 T_1 + a_3 \ln T_1) \times 10^{-6}$, where T_1 is the specific temperature, and $a_1 = 23.75$, $a_2 = 3.76 \times 10^{-3}$ and $a_3 = 5.11$.

C. V-I Characteristics of the MOSA

Electrical properties of the ZnO are described through a nonlinear V-I characteristics as shown in Fig. 2. This nonlinear behavior of ZnO ceramics is the result of the double Schottky barriers at the grain boundaries. An important parameter, which is crucial for the application of the MOSA is the clamping voltage, U_{clamp} which is set to 1.5 p.u. When the MOSA voltage exceeds the clamping voltage, U_{clamp} , it becomes highly conductive resulting in a high current flow. $U_I = 1 \text{ mA}$ is the reference voltage, which is the knee point of the characteristic curve, transition from highly insulating to conducting condition [28], [29]. $U_I = 10 \text{ kA}$ is the residual voltage at 10 kA discharge current [28]. In this work, MOSA curve is aggregated representing 12 parallel MOSA columns which correspond to the

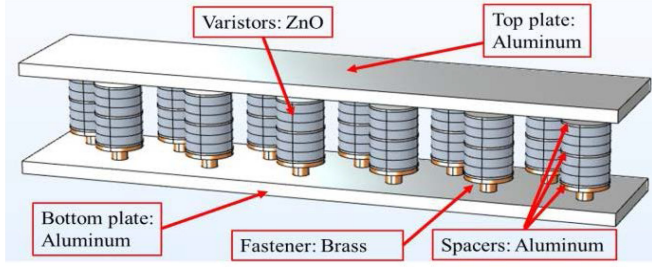


Fig. 3. Surge arrester structure and materials.

designed MOSA for the prototype dc CB that will be explained in the next section. The MOSA module is designed to have a clamping voltage of 40 kV, which corresponds to 1.5 p.u. of the nominal dc voltage. The 1 p.u. dc voltage in the presented research work is equal to 27 kV. The current density through the ZnO varistor element is determined by:

$$J(E) = \begin{cases} \frac{A_1}{\rho_{gb}} \exp\left(-\frac{E_g - \beta\sqrt{E}}{k_b T}\right) + A_2 \left(\frac{E}{E_B}\right)^\alpha & J(E) < J_U \\ D(T, J) \cdot \frac{A_3}{\rho_g} (E - E_U) + J_U & J(E) > J_U \end{cases} \quad (12)$$

In (12), J denotes the current density expressed in A/cm^2 , E is the voltage gradient in V/cm , and A_1 and A_3 are constant coefficients in units of V/cm whilst A_2 is a constant in A/cm^2 . Furthermore, ρ_{gb} is the pre-breakdown resistivity in $\Omega \cdot cm$, E_g is the height of double Schottky barriers with the value of 0.8 eV, β is a constant that deals with the electrical properties and geometrical structure of the intergranular layer of the ZnO varistors.

Moreover, e is the electron charge, $\epsilon_0 = 8.85 \times 10^{-12}$ F/m, ϵ_r is the relative dielectric constant of intergranular layer, which is in the range of 4 to 25 [22] [30]. And it is chosen with a value of $\epsilon_r = 8$ used in the model; and d is the thickness of the intergranular layer of ZnO varistors, which in practice is 120 nm. k_b is Boltzmann's constant, and $k_b = 1.38 \times 10^{-23}$ J/K, the value of $\beta = 2.83 \times 10^{-2}$ eV^{1/2}, T is the absolute temperature expressed in K, E_B is the barrier voltage of the element boundary. The remaining coefficients are: α is the nonlinear coefficient expressed as $\alpha = d(\log J)/d(\log E)$, $D(T, J)$ is a function of temperature and current density, which is obtained from experiments. E_U is the upturn voltage, $E_U = E_B (J_U/A_2)^{1/\alpha}$, where $J_U = 1 \times 10^4 A/cm^2$, is the upturn current density. In the applied model, these parameters can be changed in a way to satisfy the electrical properties of different ZnO varistors.

$$\beta = \sqrt{\frac{e^3}{4\pi d \epsilon_0 \epsilon_r}} \quad (13)$$

D. Geometry of MOSA Module

Fig. 3 illustrates the physical arrangement of the MOSA columns in a module. The MOSA module comprises two flat terminal aluminum plates, 12 ZnO varistor columns in parallel. Each ZnO varistor column consists of 6 ZnO varistor discs stacked in series, along with spacers and a mechanical fastener. The geometrical parameters - the diameter, the height and the

length of each column are required to perform the modelling and simulation.

In order to study the effect of temperature on the $V-I$ characteristics of the MOSA, it is necessary to ensure that each column has adequately matched $V-I$ characteristic. When a certain number of ZnO varistors are stacked in series to form a ZnO varistor column, the difference in aggregate $V-I$ characteristics between parallel columns can become significant. This results in non-uniform current distribution among the arrester columns which leads to non-uniform temperature rise, which may in turn result in destruction of the columns exposed to higher temperature. Therefore, matching the MOSA column $V-I$ characteristics is important in order to minimize the impact of the dispersion of the manufacturing process. This can be achieved by performing the column matching procedure.

The matching procedure is performed by applying 8/20 μs impulse to the parallel arrangement of several columns in which one is taken as a reference column. Then, the resulting impulse current flowing in each column is compared against the impulse current in the reference column. Considering the residual voltage printed on the varistor blocks, there are 10 sets of varistors with residual voltages ranging from 7.35 kV to 7.44 kV. Thus, these varistors are combined and arranged into six groups as shown in Table I. As can be seen from this table, the columns are built in such a way that the total sum of the residual voltages of each column is equal (44.37 kV).

The data about geometrical parameters, which are needed for the FE analysis are summarized in Table II. It should be pointed out that since the MOSA module is designed for indoor experimentation and providing access for temperature monitoring, there was no housing placed on the MOSA columns. In practice, polymer or porcelain housing is used to increase the dielectric strength and to protect the varistors. Whole solid-insulated MOSA are widely used for energy absorption in DC circuit breaker because of the good performance in heat dissipation. The model proposed in this paper can be applied on other types of solid-insulated ZnO. The heat conduction, heat convection and heat radiation equations can be applied on housing and other insulation materials by changing the parameters of the corresponding material characteristics.

E. Characteristics of Materials

Energy absorption process can be described by the temperature change with respect to the type of the ZnO material. As shown in Fig. 3, the varistor material is ZnO and the terminals and spacers are made of aluminum, whilst the mechanical fasteners are made of brass. The variables in Table III are temperature dependent parameters, which are available in the COMSOL default library.

F. Determination of Energy Injection

In order to obtain the amount of energy injected in the MOSA columns, the current in each column of MOSA is measured independently. Thereafter, the power (P_{SA}) and the energy (E_{SA}) corresponding to these currents can be computed by equations (14) and (15) respectively. It must be noted that

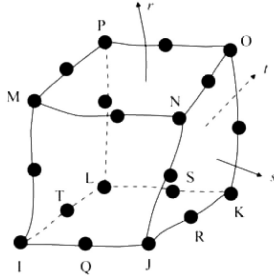


Fig. 4. 20 node hexahedra element [31].

the FE analysis is performed with variable voltage, current, and power. The total current across the MOSAs is computed by (16).

$$P_{SA}(t) = V_{SA}(t) \cdot I_{SA}(t) \quad (14)$$

$$E_{SA} = \int_0^t P_{SA}(t) dt \quad (15)$$

$$I_{SA}(t) = \sum_{i=1}^{12} I_{SA_i}(t) \quad (16)$$

The parallel connection of MOSA columns implies that they are stressed by the same voltage. Even though the MO varistor blocks are macroscopically the same, V-I characteristics may be slightly different due to manufacturing imperfections that cannot guarantee exactly identical blocks. This results in different current flows and different energy absorptions. Due to lack of data for each module of the applied MOSA, the same characteristics for each module is used. Furthermore, our objective is to analyze the temperature variation of each MOSA column during different dc current interruption scenarios, and to propose suitable methodology that can be applied in practice when dealing with thermal analysis of MOSA during dc current interruption. The proposed model can be used for MOSA columns with different geometry as well as different electrical characteristics.

G. Mesh and Simulation Time Step

The mesh division method and its fineness have an important influence on the accuracy of the calculation results. The constituents of MOSA model are relatively regular and can be meshed using free meshing methods. When dividing the computational domain, a 20-node six-sided cell is chosen to ensure high accuracy, with each node of the cell having only one degree of freedom for temperature. Fig. 4 shows a 20-node six-sided cell, whose temperature distribution function can be expressed as (17) [31][32], where r , s , t are coordinates in 3 directions respectively. And T_X ($X = I, Q, J, \dots$) is the temperature of node X .

$$\begin{aligned} T = & \frac{1}{8}(T_I(1-s)(1-t)(1-r)(-s-t-r-2) \\ & + T_J(1+s)(1-t)(1-r)(s-t-r-2) + \dots) \\ & + \frac{1}{4}(T_R(1+s)(1-t^2)(1-r) + T_S(1-s) \\ & \times (1-t^2)(1-r) + \dots) \end{aligned} \quad (17)$$

Transient heat conduction equation (1) can be transformed into a transient heat balance equation with the nodal temperature expressed as:

$$\mathbf{C} \dot{\mathbf{T}} + \mathbf{K}\mathbf{T} = \mathbf{Q}(\mathbf{T}) \quad (18)$$

where \mathbf{C} is heat capacity matrix; \mathbf{K} is heat conductivity matrix; \mathbf{T} is temperature matrix; $\dot{\mathbf{T}}$ is the derivative matrix of temperature with respect to time, and \mathbf{Q} is the heat load matrix, which is temperature dependent.

By utilizing the Euler equation, the temperature at every instant t can be calculated from the temperature at the previous instant $t-1$.

$$\mathbf{T}^t = \mathbf{T}^{t-1} + (1-\theta)\Delta t \dot{\mathbf{T}}^{t-1} + \theta\Delta t \dot{\mathbf{T}}^t \quad (19)$$

where θ is the Euler parameter; Δt is the time step and for the implicit Euler equation, $0.5 \leq \theta \leq 1$. Accurate results are strongly dependent on the correct time step applied in the FE analysis. As FE simulation deals with the solution of a system of partial differential equations by taking into account different boundary conditions, the experience shows that the smaller the time step is, the more accurate the results are. Depending on the dc CBs, the dc current interruption process lasts several milliseconds and the energy absorption process usually takes 5–10 ms. In the present case, a simulation time step of 10 μ s for the energy absorption process is used, which is sufficient to obtain accurate results as it was validated later through the experimental measurements. This is to take in to account the high frequency oscillation occurring in the MOSA voltage and current especially during the initial stage of the current commutation into the MOSA branch. Besides, the temperature decay lasts for several tens of minutes, and therefore, the FE simulation may take very long time when using the same time step. Hence, for the temperature decay, large time steps are applied. In this way, the computational procedure is conducted in two steps. Firstly, the energy absorption is computed by making use of small-time steps (in the order of 10 μ s), and thereafter, the temperature decay is computed with larger time steps (order of several seconds). This offers possibility in the future studies to accelerate the computation process in case when having multiple reclosing scenarios of the dc CBs.

III. EXPERIMENTAL SETUP

A. Description of the Experimental Test Setup

The test circuit that is used to perform dc CB current interruption is illustrated in Fig. 5 and it has been verified in [33], [34]. The test circuit is energized by a low frequency ac short-circuit generator, which operate at 16.7 Hz. The making switch (MS) controls the current making angle and the master breaker (MB) controls the supply of low-frequency sinusoidal current, where only a half cycle is needed. The MB will interrupt the supplied current at the first natural current zero-crossing in case the dc CB fails to clear. In order to limit the rate of rise of the current, an adjustable reactor is used. For the dc current interruption, an active injection dc CB is utilized and as previously described in Fig. 1, the applied dc CB consists

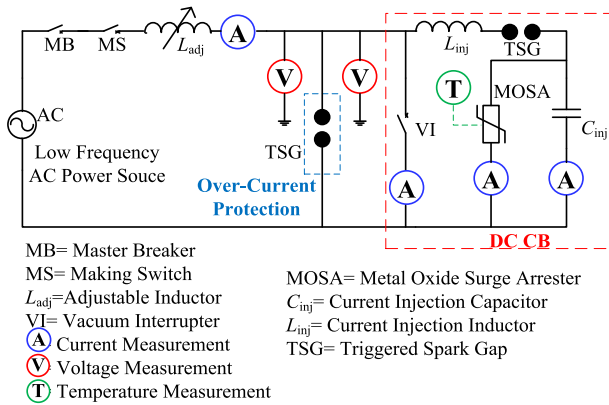


Fig. 5. Equivalent test circuit for dc CB energy absorption.

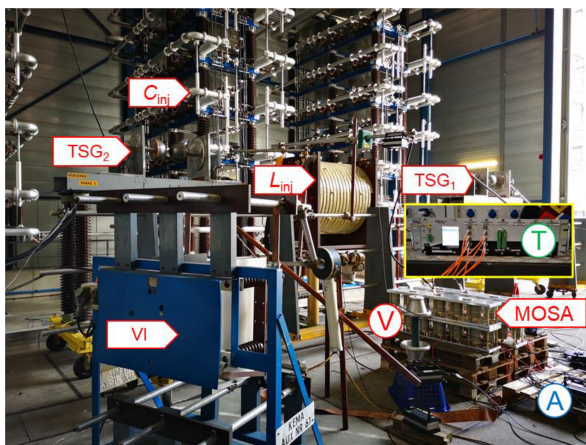


Fig. 6. Laboratory setup of the dc CB components.

of three branches: the main branch, the current commutation branch, and the energy absorption branch. The main branch is a vacuum circuit breaker (VCB) rated at a voltage of 36 kV and a breaking current of 40 kA. The VCB is actuated by a spring mechanism providing an opening time of 46.6 ms. The opening time of the breaker is the duration between received trip signal and the instant of contact separation, which is precisely known before the experiment takes place. Hence, the trip signal of MS, the VCB and the triggered spark gap (TSG_2) can be precisely sequenced. The active injection branch comprises of a pre-charged current injection capacitor (C_{inj}), a current injection inductor (L_{inj}) and a TSG_2 . The energy absorption branch consists of twelve MOSA columns. The laboratory set up of the main dc CB components can be seen in Fig. 6.

As the scope of the paper is the energy absorption by the MOSAs in dc CB during interruption, the dc CB topology and the driving mechanism or the fault current clearing time are beyond the scope. Therefore, more details can be found in [34].

B. Measurements

During the experimental campaign, several MOSA parameters were monitored, and the following measurements have been recorded:

- Voltage across the VI

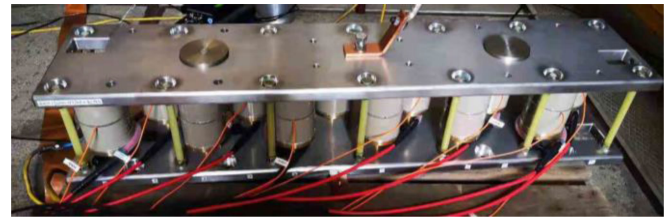


Fig. 7. Surge arrester measurement and surge arrester prototype.

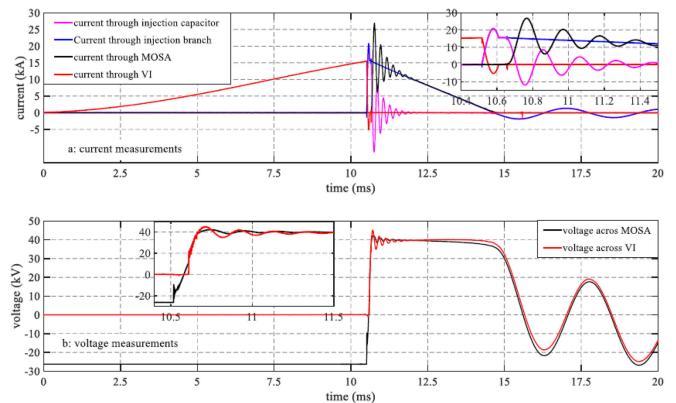


Fig. 8. Typical test results of current through and voltage across MOSA.

- Current through the VI
- Voltage across the MOSA
- Total current through the MOSA
- Current through eight columns of MOSA
- Temperature measurement of eight columns of MOSA (the same columns in which current measurements were taken)

A multi-channel fiber optic-based based temperature measurement system with data acquisition rate as high as 10 Hz per channel is used. This system is Qualitrol, Neoptix OmniFlex-2 temperature measurement system as shown in zoom in Fig. 6. Fig. 7 shows the MOSA module with eight mounted fiber optic-based temperature sensors. The sensors are placed at the center of each column since this is typically the hottest spot.

IV. RESULTS AND ANALYSIS

A. Typical Test Results of MOSA Voltage and Current

Fig. 8 depicts a typical test result showing the current commutation in the MOSA branch. The negative voltage across the MOSA is a pre-charged voltage across the injection capacitor applied to the MOSA as well.

Firstly, the current is cleared by the VI at the 2nd high-frequency current zero crossing. Thereafter, the injection branch is activated where the current commutes to and charges the capacitor. When the voltage across the capacitor reaches around 35 kV, the MOSA begins to conduct, and the system current commutates from the capacitor to the MOSA (which is indicated by the magenta and the black trace in the zoomed part of Fig. 8). However, the commutation does not stop until the MOSA current equals the system current. Instead, the MOSA current continues to increase to a higher value than the system current. This is

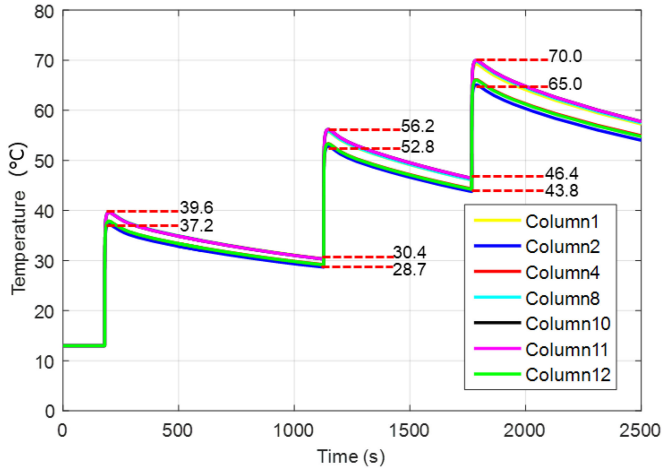


Fig. 9. Simulation results of MOSA temperature variation.

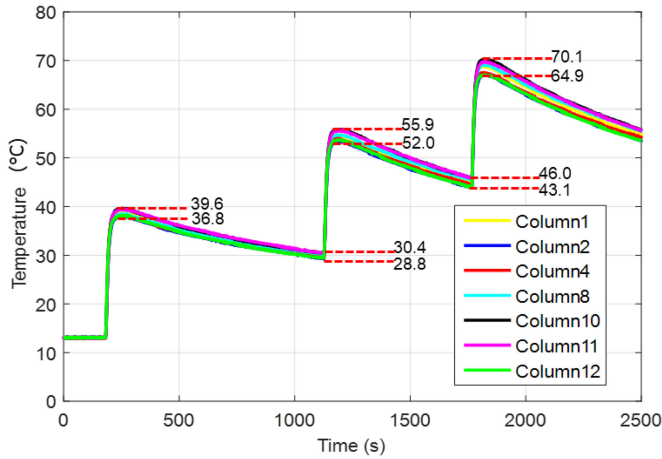


Fig. 10. Experimental results of MOSA temperature variation.

due to the loop stray inductance between the injection capacitor and the MOSA, where a circulating current flow. This is well visible in the decaying oscillation of the MOSA and capacitor current measurements. This oscillation is not observed in the system current. This circulating current results in an oscillating capacitor charge and a TIV, which may be reduced by a compact (low inductance) design of the set-up. The difference in the voltage measurements across the VI and the MOSA is due to the voltage drop across the stray inductance of the measurement loop. In this case, the MOSA conducts for about 4 ms whilst maintaining the voltage above 38 kV. During this time, the absorbed energy from the MOSA is about 1.3 MJ.

B. Successive DC Interruption and MOSA Temperature Variation

Three successive dc current interruptions are carried out, for which the measured energy absorption in each test is about 850 kJ. The ambient temperature during the test was 13 °C. Fig. 9 and Fig. 10 show the simulated results and the experimental results of the MOSA temperature variation, respectively. The first current interruption occurs at $t = 183.0$ s. From 183.0 s to 183.3 s, the

TABLE IV
ENERGY ABSORPTION IN EACH MOSA COLUMN

Energy/ kJ	1 st interruption	2 nd interruption	3 rd interruption
Column 1	71.42	72.03	70.92
Column 2	69.12	70.75	70.24
Column 4	71.04	71.31	70.82
Column 8	75.87	76.5	75.19
Column 10	76.43	76.62	74.87
Column 11	75.74	76.17	75.36
Column 12	73.84	74.63	73.44

MOSAs temperature abruptly rises because this period the heat is transferred from ZnO varistors to the aluminum disc in which the fiber optic-based temperature sensors are inserted, and the MOSAs reaches the first peak value of 39.6 °C. As soon as the MOSA energy absorption is finished, the temperature decays slowly. The heat in the MOSA columns begins to diffuse into the environment of the MOSA which undergoes a heat conduction process. The second interruption occurs at $t = 1127.0$ s and the third interruption at $t = 1767.0$ s, respectively. The energy absorbed in each column for all three interruptions is shown in Table IV. As we can see from the results, columns 8, 10 and 11 absorb more energy than the other columns. As a result, the temperature rise in these three columns is higher than that of the others.

During the first current interruption, the temperature difference between the local maximum and minimum temperature is 1.8 °C; and for the second interruption and the third interruption, the maximum and the minimum difference is 3.9 °C and 5.2 °C. After 3 successive interruptions, the MOSA columns are at a higher average temperature, and a greater difference exist between maximum and minimum temperature. The difference between the experimental results and the simulation results, which is mainly due to the assumptions in the simulation is 1.4%.

In this experimental work, the currents through 8 MOSA columns are also measured for three successive dc current interruptions. The currents through the MOSA columns for the first dc current interruption and for the third dc current interruption are presented in Fig. 11 and Fig. 12, respectively, and imply that the current through the MOSA columns is not equally distributed.

Especially, the deviation between the column currents increases as the MOSA temperature increases. The temperature difference is enlarged due to differences in the cooling of MOSA columns caused by the physical arrangement of the columns. The columns which are located in the middle along the length of the MOSA module have less ventilation compared to those located at the edges.

The temperature distribution among the ZnO varistor columns after the 3rd current interruption is shown in Fig. 13.

The current distribution uniformity B is expressed as a ratio between the maximum and the average current among all ZnO

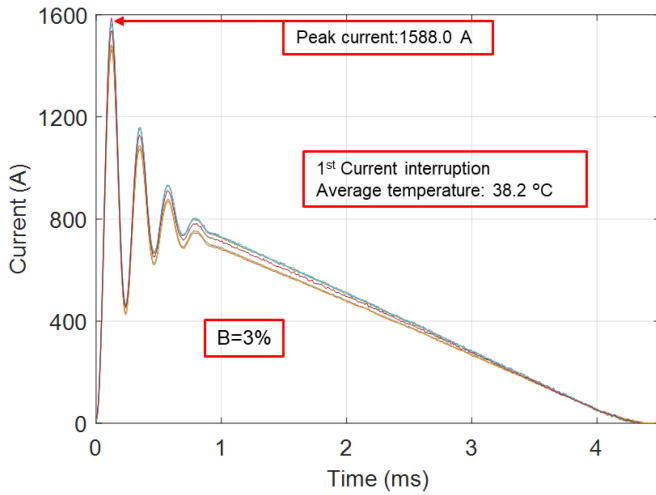


Fig. 11. Measured current distribution among MOSA columns during 1st energy absorption.

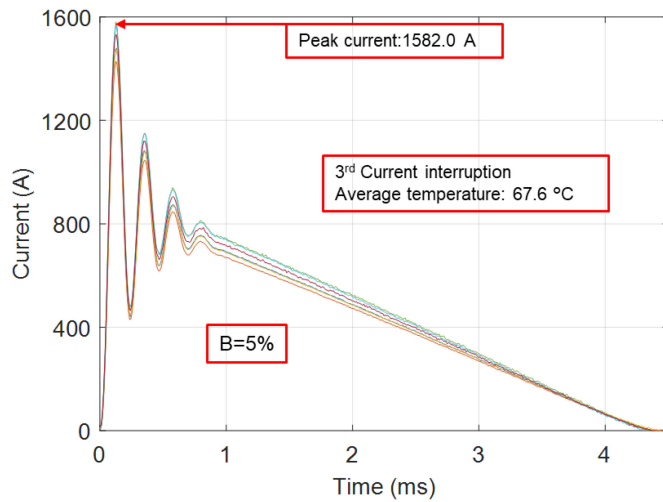


Fig. 12. Measured current distribution among MOSA columns during 3rd energy absorption.

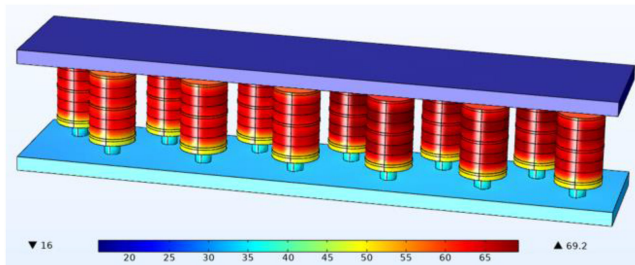


Fig. 13. Simulation result of temperature distribution after 3rd current interruption.

varistor columns, (I_{\max}) and (I_{ave}), respectively:

$$B = \frac{I_{\max} - I_{\text{ave}}}{I_{\text{ave}}} \quad (20)$$

The difference of the maximum temperature and the average temperature can be computed by (5), (10) and (12) as (13). The

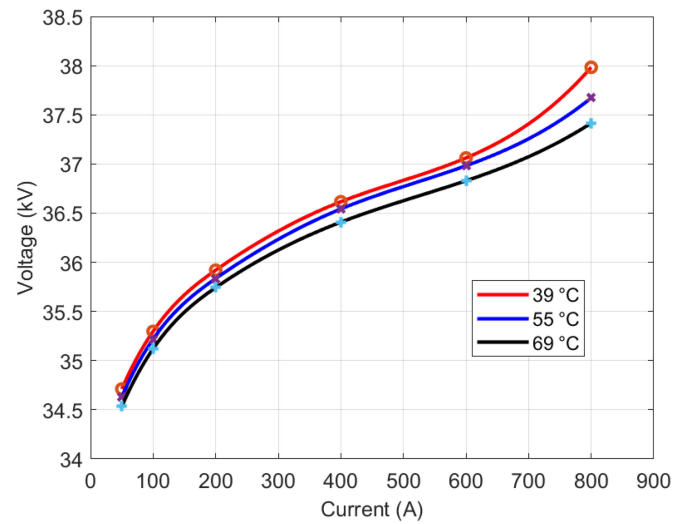


Fig. 14. Test results of V-I characteristic during three interruptions.

temperature difference can be estimated as BE_{ave} , if the impact of temperature on density and heat capacity is neglected.

$$\Delta T_{\max} - \Delta T_{\text{ave}} = \frac{E_{\max}}{V \rho_{\max} C_{P_{\max}}} - \frac{E_{\text{ave}}}{V \rho_{\text{ave}} C_{P_{\text{ave}}}} \approx BE_{\text{ave}} \quad (21)$$

The temperature difference between columns leads to more non-uniform current distribution, which results in greater temperature difference. As a result of this, MOSA failure may take place after several current interruptions. Meanwhile, the negative temperature-resistivity characteristic of ZnO varistors also contributes to a greater difference. As shown in Fig. 14, the V-I characteristic of one column during the third interruption with different temperature are compared. With the increase of MOSA temperature, the voltage required to generate the same current decreases. In the high-current region, the temperature has more impact on the voltage for the same current, whilst in the low-current region, the temperature difference has less impact on the V-I characteristic. $D(69^\circ\text{C}, 800\text{A}) = -0.020^\circ\text{C/kV}$, which is verified by the test results in [35].

C. Cracking

The mechanical pressure inside the ZnO varistors during the temperature variation is shown in Fig. 15. The open circles in Fig. 15 are simulation results, and the line is the relation between the temperature rise and mechanical pressure. The critical thermal stress F_c , which is capable of cracking the varistor is in the range of 48.3 MPa [22] to 100 MPa [23]. The value of 48.3 MPa is chosen as the safe operation threshold of the ZnO, for which the corresponding temperature is 150 °C.

Furthermore, MOSA destruction tests are carried out with four successive current interruptions, until the cracking failure takes place. The temperature variation during MOSA destruction tests is shown in Fig. 16. The energy absorbed by MOSA in first three tests is 2.59 MJ, 2.68 MJ and 2.64 MJ, respectively. Meanwhile, the temperature variation of MOSA in first three tests is 72.0 °C, 68.6 °C and 66.3 °C, respectively. The fourth test is carried

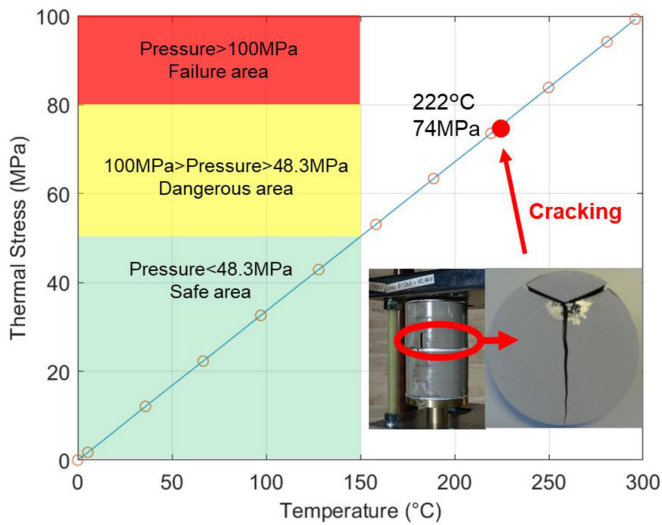


Fig. 15. Thermal stress inside surge arrester influence by temperature.

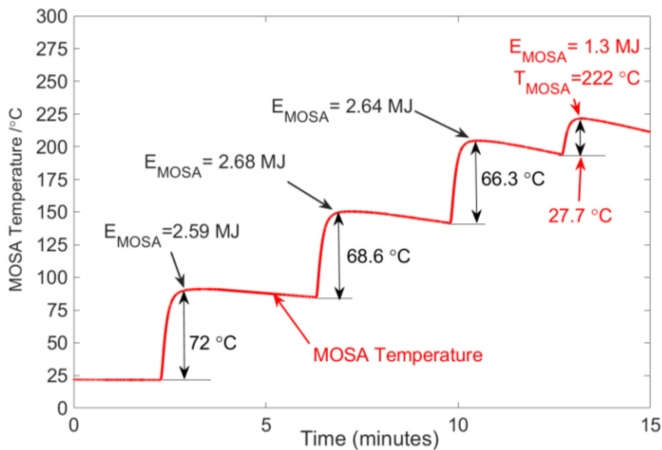


Fig. 16. Temperature measurement during MOSA destruction tests.

out at 12.7 minute, at which time the MOSA temperature is 194.3 °C. The MOSA absorbs the energy normally for 2.2 ms, then failure occurs. At instant of failure, the MOSA temperature is 222 °C, the voltage across MOSA is 38.5 kV and the current through MOSA is 10.6 kA. The cracking destruction occurs at $T = 222$ °C, a temperature for which the corresponding thermal stress is 74 MPa.

V. CONCLUSION

The paper presents the thermal behavior of MOSA resulting from dc current interruption realized with active current injection dc CB. The model is built by making use of the fluid dynamics equations in powerful COMSOL. The focus of the work is to analyze the energy absorption process and heat diffusion in the MOSA modules, and it can be used to identify the hot spots in the MOSA. The model offers large scale flexibility, and each MOSA module can be modeled by different V-I characteristic and different geometry as long as it is necessary. The computation process is conducted in two stages, which comprise small and large time steps during fast temperature rise and very

slow temperature decay, respectively. The computed results are qualitatively compared by unique experimental results where the measurements are conducted by utilizing mounted fiber optic-based temperature sensors. The computed and the experimental results are in good agreement, which verifies the validity of the MOSA thermal model.

The deviation between the column currents increases as the temperature of the MOSA increases. The temperature difference is enlarged due to differences in the cooling of MOSA columns caused by the arrangement of the columns. As the columns located in the middle have less convection losses compared to the peripheral columns, larger temperature difference exists. In the high-current region, the temperature has higher impact on the voltage amplitude for the same current value. The performed analysis can be used for every dc CB to evaluate the performance of the MOSAs, which play an important role for the successful operation of the dc CBs.

ACKNOWLEDGMENT

The authors would like to acknowledge the support of KEMA testing team in the ‘PROMOTioN’ project for helping with the measurements and using their facilities. They also acknowledge the support of Peter Hock and his team from Technology University Darmstadt for designing and building the MOSA modules used in the experiment. The first author thanks Delft University of Technology for providing an opportunity and a position to conduct research in the frame of PROMOTioN project. Finally, they highly acknowledge the comprehensive comments and constructive advice of the anonymous reviewers who helped bringing the paper to this form.

REFERENCES

- [1] M. Cheah-Mane, L. Sainz, J. Liang, N. Jenkins, and C. E. Ugalde-Loo, “Criterion for the electrical resonance stability of offshore wind power plants connected through HVDC links,” *IEEE Trans. Power Syst.*, vol. 32, no. 6, pp. 4579–4589, Nov. 2017.
- [2] Y. Pipelzadeh, N. R. Chaudhuri, B. Chaudhuri, and T. C. Green, “Coordinated control of offshore wind farm and onshore HVDC converter for effective power oscillation damping,” *IEEE Trans. Power Syst.*, vol. 32, no. 3, pp. 1860–1872, May 2017.
- [3] R. Ferdinand, and A. Monti, “Export transformer switching transient mitigation in HVDC connected offshore wind farms,” *IEEE Trans. Power Del.*, vol. 35, no. 1, pp. 37–46, Feb. 2020.
- [4] S. Liu *et al.*, “Modeling, experimental validation, and application of VARC HVDC circuit breakers,” *IEEE Trans. Power Del.*, vol. 35, no. 3, pp. 1515–1526, Jun. 2020.
- [5] C. M. Franck, “HVDC circuit breakers: A review identifying future research needs,” *IEEE Trans. Power Del.*, vol. 26, no. 2, pp. 998–1007, Apr. 2011.
- [6] L. Angquist, A. Baudoin, S. Norrga, S. Nee, and T. Modeer, “Low-cost ultra-fast DC circuit-breaker: Power electronics integrated with mechanical switchgear,” in *Proc. IEEE Int. Conf. Ind. Technol.*, 2018, pp. 1708–1713.
- [7] K. Tahata *et al.*, “HVDC circuit breakers for HVDC grid applications,” in *Proc. 11th IET Int. Conf. AC DC Power Trans.*, Birmingham, U.K., 2015, pp. 1–9.
- [8] X. Song, C. Peng, and A. Q. Huang, “A medium-voltage hybrid DC circuit breaker, part I: Solid-state main breaker based on 15 kV SiC emitter Turn-OFF thyristor,” *IEEE J. Emerg. Sel. Top. Power Electron.*, vol. 5, no. 1, pp. 278–288, Mar. 2017.
- [9] T. Wei *et al.*, “Design and test of the bidirectional solid-state switch for an 160 kV/9 kA hybrid DC circuit breaker,” in *Proc. IEEE Appl. Power Electron. Conf. Expo.*, 2018, doi: [10.1109/APEC.2018.8341000](https://doi.org/10.1109/APEC.2018.8341000).

- [10] L. Liu, J. Zhuang, C. Wang, Z. Jiang, J. Wu, and B. Chen, "A hybrid DC vacuum circuit breaker for medium voltage: Principle and first measurements," *IEEE Trans. Power Del.*, vol. 30, no. 5, pp. 2096–2101, Oct. 2015.
- [11] E. Kontos *et al.*, "Multiline breaker for HVdc applications," *IEEE Trans. Power Del.*, vol. 33, no. 3, pp. 1469–1478, Jun. 2018.
- [12] J. Häfner and B. Jacobson, "Proactive hybrid HVDC breakers - A key innovation for reliable HVDC grids," presented at the Cigre Int. Symp., Bologna, Italy, Sep. 2011, Paper 264.
- [13] X. Han, W. Sima, M. Yang, L. Li, T. Yuan, and Y. Si, "Transient characteristics under ground and short-circuit faults in a 500 kV MMC-based HVDC system with hybrid DC circuit breakers," *IEEE Trans. Power Del.*, vol. 33, no. 3, pp. 1378–1387, Jun. 2018.
- [14] N. A. Belda, C. A. Plet, and R. P. P. Smeets, "Analysis of faults in multiterminal HVDC grid for definition of test requirements of HVDC circuit breakers," *IEEE Trans. Power Del.*, vol. 33, no. 1, pp. 403–411, Feb. 2018.
- [15] R. Sander and T. Leibfried, "Considerations on energy absorption of HVDC circuit breakers," in *Proc. Univ. Power Eng. Conf.*, 2014, pp. 1–6.
- [16] S. Liu and M. Popov, "Development of HVDC system-level mechanical circuit breaker model," *Int. J. Electric Power Energy Syst.*, vol. 103, pp. 159–167, Dec. 2018.
- [17] M. Bartkowiak, M. G. Comber, and G. D. Mahan, "Influence of nonuniformity of ZnO varistors on their energy absorption capability," *IEEE Power Eng. Rev.*, vol. 21, no. 7, Jul. 2001, Art. no. 69.
- [18] J. He, J. Lin, W. Liu, H. Wang, Y. Liao, and S. Li, "Structure-dominated failure of surge arresters by successive impulses," *IEEE Trans. Power Del.*, vol. 32, no. 4, pp. 1907–1914, Aug. 2017.
- [19] L. Huang and M. R. Raghuveer, "Hybrid simulation of metal oxide surge-arrester thermal behaviour," *Can. J. Electric Comput. Eng.*, vol. 21, no. 1, pp. 33–39, Jan. 1996.
- [20] S. T. Li, J. Q. He, J. J. Lin, H. Wang, W. F. Liu, and Y. L. Liao, "Electrical-Thermal failure of metal-oxide arrester by successive impulses," *IEEE Trans. Power Del.*, vol. 31, no. 6, pp. 2538–2545, Dec. 2016.
- [21] Y. Spack-Leigsnering, E. Gjonaj, H. De Gerssem, T. Weiland, M. Giebel, and V. Hinrichsen, "Electroquasistatic-thermal modeling and simulation of station class surge arresters," *IEEE Trans. Magn.*, vol. 52, no. 3, Mar. 2016, Art no. 9100104.
- [22] J. L. He, and J. Hu, "Discussions on nonuniformity of energy absorption capabilities of ZnO varistors," *IEEE Trans. Power Del.*, vol. 22, no. 3, pp. 1523–1532, Jul. 2007.
- [23] M. Bartkowiak, M. G. Comber, and G. D. Mahan, "Failure modes and energy absorption capability of ZnO varistors," *IEEE Trans. Power Del.*, vol. 14, no. 1, pp. 152–160, Jan. 1999.
- [24] Y. Huang, K. Wu, Z. Tang, L. Xin, L. Zhang, and J. Li, "Investigation of electrical inhomogeneity in ZnO varistor ceramics based on electronic relaxations," *Ceram. Int.*, vol. 45, no. 1, pp. 1110–1114, 2019.
- [25] Z. Topcagic, T. Tsovilis, and D. Krizaj, "Modeling of current distribution in zinc oxide varistors using voronoi network and finite element method," *Electric Power Syst. Res.*, vol. 164, pp. 253–262, Nov. 2018.
- [26] Z. Topcagic, M. Mlakar, and T. E. Tsovilis, "Electrothermal and overload performance of metal-oxide varistors," *IEEE Trans. Power Del.*, vol. 35, no. 3, pp. 1180–1188, Jun. 2020.
- [27] J. He, R. Zeng, and S. Chen, "Thermal characteristics of high voltage whole-solid-insulated polymeric ZnO surge arrester," *IEEE Trans. Power Del.*, vol. 18, no. 4, pp. 1221–1227, Oct. 2003.
- [28] B. Richter, "Application guidelines: Overvoltage protection metal-oxide surge arresters in medium-voltage systems," *ABB Switz. Ltd.*, 2018, Art. no. 12.
- [29] *Metal-Oxide Surge Arresters Without Gaps For A.C. Systems*, IEC Standard 60099-4, 2014.
- [30] L. M. Levinson and H. R. Philipp, "The physics of metal oxide varistors," *J. Appl. Phys.*, vol. 46, no. 3, pp. 1332–1341, 1975.
- [31] Z. He *et al.*, "Calculation method for transient thermal characteristics of Multi-column parallel structure surge arrester," *High Volt. Eng.*, vol. 38, no. 8, pp. 2129–2136, 2012.
- [32] Cigré Working Group A3.25, "MO surge arresters: Metal oxide varistors and surge arresters for emerging system conditions," Tech. Brochure 696, 2017.
- [33] N. A. Belda, C. Plet, and R. P. P. Smeets, "Full-Power test of HVDC circuit-breakers with ac short-circuit generators operated at low power frequency," *IEEE Trans. Power Del.*, vol. 34, no. 5, pp. 1843–1852, Oct. 2019.
- [34] N. A. Belda, R. P. P. Smeets, and R. M. Nijman, "Experimental investigation of electrical stresses on the main components of HVDC circuit breakers," *IEEE Trans. Power Del.*, vol. 1, no. 1, pp. 1–10, Dec. 2020.
- [35] H. Cai, C. Liao, and J. Guo, "Research of metal oxide surge arrester V–A temperature characteristics," *Insul. Surge Arresters*, vol. 2019, no. 4, pp. 3–7, 2019.



Siyuan Liu (Member, IEEE) received the B.Sc. degree in electrical engineering from the Harbin Institute of Technology, Harbin, China, in 2013 and the Ph.D. degree in electrical engineering from Xi'an Jiaotong University, Xi'an, China, in 2020. From 2016 to 2020, he was a Researcher with the Delft University of Technology, Delft, The Netherlands. Since 2021, he has been with the State Key Laboratory of Electrical Insulation and Power Equipment, Department of Electrical Engineering, Xi'an Jiaotong University, where he is currently an Assistant Professor. His research interests include HVDC circuit breakers, protection and transients in MTDC grids, and vacuum interrupter theory and application. He is selected for China National Postdoctoral Program for Innovative Talents.



Marjan Popov (Senior Member, IEEE) received the Ph.D. degree in electrical power engineering from the Delft University of Technology, Delft, The Netherlands, in 2002. He is also a Chevening Alumnus and in 1997, he was an Academic Visitor with the University of Liverpool, Liverpool, U.K., working with Arc Research Group on modeling SF6 circuit breakers. His main research interests include future power systems, large-scale power system transients, intelligent protection for future power systems, and wide-area monitoring and protection. He is a Member of Cigre and actively participated in WG C4.502 and WG A2/C4.39. In 2010, he was the recipient of the prestigious Dutch Hidde Nijland Prize for extraordinary research achievements. He was also the recipient of the IEEE PES Prize Paper Award and IEEE Switchgear Committee Award in 2011 and an Associate Editor for the *Elsevier's International Journal of Electrical Power and Energy Systems*. In 2017, together with the Dutch utilities TenneT, Alliander and Stedin he founded the Dutch Power System Protection Centre to promote the research and education in power system protection.

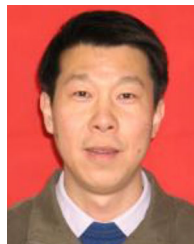


Nadew Adisu Belda (Member, IEEE) received the B.Sc. degree in electrical engineering from Bahir Dar University, Bahir Dar, Ethiopia, in 2009, the M.Sc. degree in communication engineering from Addis Ababa University, Addis Ababa, Ethiopia, in 2011, and the joint M.Sc. degrees (*Cum Laude*) in electrical power engineering from the Eindhoven University of Technology, Eindhoven, The Netherlands, and the Royal Institute of Technology, Stockholm, Sweden, in 2015. He is currently working toward the Ph.D. degree with Technische Universität Darmstadt, Darmstadt, Germany. He is currently with KEMA Laboratories, Innovation Department, responsible for the development of test methods and design of test circuits for HVDC switchgear. His research interests include HVDC switchgear with a focus on HVDC circuit breakers and investigation of transients in multiterminal HVDC system.



René Peter Paul Smeets (Fellow, IEEE) received the Ph.D. degree for research work on switchgear, in 1987. Until 1995, he was an Assistant Professor with Eindhoven University, The Netherlands. During 1991, he was with Toshiba Corporation, Japan. In 1995, he joined KEMA, The Netherlands. He is currently with KEMA Laboratories of CESI Group, as an Innovation and Technology Specialist. In 2001, he was appointed part-time Professor with Eindhoven University. In 2013, he became an Adjunct Professor with Xi'an Jiaotong University, China.

He is convener or a member of working groups and study or advisory committees of CIGRE in the field of emerging technologies, such as HVDC switchgear and SF6 alternatives. He is convener of two maintenance teams in IEC on high-voltage switchgear. He was a work package leader of the EU project PROMOTioN, committed to demonstrated the full-power testing of HVDC circuit breakers. He has authored or coauthored and edited three books and authored more than 300 international papers on testing and switching in power systems. Since 2008, he has been the Chairman of the Current Zero Club, a scientific study committee on current interruption. He was the recipient of eight international awards.



Zhiyuan Liu (Senior Member, IEEE) was born in Shenyang, China, in 1971. He received the B.S. and M.S. degrees in electrical engineering from the Shenyang University of Technology, Shenyang, China, in 1994 and 1997, respectively, and the Ph.D. degree in electrical engineering from Xi'an Jiaotong University, Xi'an, China, in 2001. From 2001 to 2002, he was with the General Electric Company Research and Development Center, Shanghai, China. Since 2003, he has been with the State Key Laboratory of Electrical Insulation and Power Equipment, Xi'an

Jiaotong University, where he is currently a Professor. He has authored and coauthored two books and more than 300 technical papers. His current research interests include high-voltage vacuum circuit breakers. He is a Member of the Current Zero Club.